Nonlinear Radar via Intermodulation of Jointly Optimized FM Noise Waveform Pairs

Jonathan Owen[1], Charles Mohr[1], Shannon D. Blunt[1], Kyle Gallagher[2]
[1] Radar Systems Lab (RSL), University of Kansas, Lawrence, KS
[2] Sensors and Electron Devices Division, Army Research Laboratory (ARL), Adelphi, MD

***Abstract*—It was recently shown that a new form of nonlinear radar can be achieved using pairs of separately optimized FM noise waveforms, where the optimization serves to provide useful spectral shaping of each waveform. Here the utility of jointly designing these separately transmitted waveforms according to their resulting intermodulation response is explored. This formulation relies on gradient descent optimization of an intermodulation-based cost function that is defined in the context of physically realizable polyphase-coded FM (PCFM) waveforms. The result is evaluated both in simulation and experimentally via a hardware loopback configuration.**

Keywords—nonlinear radar, intermodulation, waveform diversity, FM noise waveforms

I. Introduction

Nonlinear radar has been investigated since the 1970s [1] for a variety of applications, a notable example of which is the detection of RF electronics such as cellular telephones and radios. With the fundamental sensing mechanism being driven by the capture of a phenomenological response at a frequency that is discernible from the interrogating signal, research has overwhelmingly focused on harmonic responses instead of intermodulation effects [2]. Specifically, for transmitted frequency f_0, the prevalent class of approaches is denoted as *harmonic radar* and seeks to identify the presence of harmonics $2f_0$, $3f_0$, etc. within the resulting reflections. For this detection to be meaningful, however, it is necessary to suppress similar harmonic signals that the transmitter itself may generate, thus incurring strict requirements on transmitter spectral purity [3].

By comparison, much less effort has been focused on the intermodulation of different signals (e.g. see [4, 5]). In this case, frequencies f_1 and f_2 produce intermodulation frequencies $f_1 + f_2$, $f_1 - f_2$, $2f_1 + f_2$, $2f_1 - f_2$, etc. that are distinct from the individual harmonics of $2f_1$, $2f_2$ and so on. Intermodulation approaches have generally been viewed as more limited than harmonic approaches because RF devices tend to contain a front-end bandpass filter [5, 6] that confines the bandwidth over which a nonlinear response can be elicited. The two interrogating signals can only be separated by a limited degree, which limits the frequency separability of the intermodulation response from the harmonics.

However, the recent shared-spectrum pseudo-random intermodulation (SSPRInt) approach [7] experimentally demonstrated that a large number of FM noise waveform pairs can produce a set of unique intermodulation responses over a coherent processing interval (CPI). Because these responses are distinct from the individual harmonics of each waveform, subsequent slow-time processing over the CPI facilitates coherent gain on only the intermodulation response in accordance with the number of pulse pairs.

The approach in [7] relies on the use of pseudo-random optimized FM (PRO-FM) noise waveforms [8, 9] possessing spectral shaping that provides relatively good spectral containment (to make them amenable to a high-power transmitter) and to afford acceptable range sidelobe performance on a per-pulse basis. The notion of FM noise waveforms represent a form of waveform diversity [10] that has been theoretically analyzed in [11-13] and has been employed in a variety of applications such as the realization of practical transmit spectral notches [14], separation of simultaneous co/cross-polarized emissions [15], random modulation of a spatial mainbeam during the pulse via a MIMO arrangement [16], experimental demonstration of a practical complementary capability [17], a particular form of dual-function radar/communications [18], and more.

Where the approach in [7] involves separate optimization of each random waveform in a given pulse pair, here we examine the impact of optimizing the pair in a joint manner according to their intermodulation response. In other words, given an approximate model for the expected nonlinear behavior in the form of a power series [19-21], a cost function based on the separability of the intermodulation and harmonic responses can be constructed that permits the co-design of the interrogating waveforms. The efficacy of this joint SSPRInt (or J-SSPRInt) approach is demonstrated in simulation and experimentally in a loopback configuration.

II. Joint SSPRInt Waveform Optimization

In [7] a concise discussion of the operation of the SSPRInt approach to intermodulation radar is provided and the reader is directed there for further details. Here we focus on the joint design of the unique waveform pairs. Consider a pulsed, FM waveform $s(t)$ with pulsewidth T that is defined on $t \in [0, T]$ according to the polyphase-coded FM (PCFM) model [22]

$$s(t;\mathbf{x}) = \exp\left\{ j\left(\int_0^t g(\tau) * \left[\sum_{n=1}^{N} \alpha_n \delta\big(\tau - (n-1)T_p\big) \right] d\tau \right) \right\} = \exp\{j\phi(t)\}. \quad (1)$$

Here $g(t)$ is a shaping filter with time support $[0, T_\mathrm{p}]$ such that $T = NT_\mathrm{p}$, the operation $*$ is convolution, $\delta(t)$ is an impulse function, and $\mathbf{x} = [\alpha_1\ \alpha_2 \ldots \alpha_N]^T$ contains the N parameters to optimize. Because it is composed of linear operations, the phase function in (1) can alternatively be expressed as

$$\phi(t) = \sum_{n=1}^{N} b_n(t)\alpha_n + \phi_o, \quad (2)$$

where

This work was supported by the Army Research Office under Contract # W911NF-15-2-0063.

$$b_n(t) = \int_0^t g(\tau - (n-1)T_p)d\tau \tag{3}$$

is the continuous basis function that is weighted by α_n and ϕ_o is an arbitrary phase offset. For $g(t)$ a rectangular filter, the basis functions of (3) become time-shifted ramp functions.

For the purpose of optimization, a discretization of the PCFM model in (1) is

$$\mathbf{s} = \exp(\, j\mathbf{B}\mathbf{x} + \phi_0) \tag{4}$$

in which the columns of the $L \times N$ matrix $\mathbf{B}$ are discretized versions of $b_n(t)$ and $L = KN$ is the length of $\mathbf{s}$, for K the "over-sampling" factor relative to the waveform's 3-dB bandwidth B. Note than N approximates the time-bandwidth product BT for each individual waveform. Here two signals $\mathbf{s}_1$ and $\mathbf{s}_2$ are to be jointly optimized, and the phase offsets $\phi_{\mathrm{o},1}$ and $\phi_{\mathrm{o},2}$ are drawn independently from a uniform distribution on U[0, 2π]. Thus we can write

$$\mathbf{s}_1 = \mathrm{e}^{j\mathbf{B}\mathbf{x}_1 + \phi_{\mathrm{o},1}} \tag{5}$$

$$\mathbf{s}_2 = \mathrm{e}^{j\mathbf{B}\mathbf{x}_2 + \phi_{\mathrm{o},2}}\,. \tag{6}$$

We wish to design the two phase-change codes $\mathbf{x}_1$ and $\mathbf{x}_2$ such that the corresponding discretized FM signals $\mathbf{s}_1$ and $\mathbf{s}_2$ produce *a*) an intermodulation signal $\mathbf{s}_{12}$ whose autocorrelation has minimal sidelobes and *b*) harmonic signals $\mathbf{s}_{11}$ and $\mathbf{s}_{22}$ that each have minimal cross-correlation with $\mathbf{s}_{12}$. From the power series model [19-21], and using the continuous representation from [7], the discretized form of the intermodulation and harmonic signals can be expressed as

$$\mathbf{s}_{12} = \mathbf{s}_1 \odot \mathbf{s}_2 \tag{7}$$

$$\mathbf{s}_{11} = \mathbf{s}_1 \odot \mathbf{s}_1 \tag{8}$$

$$\mathbf{s}_{22} = \mathbf{s}_2 \odot \mathbf{s}_2 \tag{9}$$

where $\odot$ is the Hadamard product.

Now append $L-1$ zeros to $\mathbf{s}_1$ and $\mathbf{s}_2$ as

$$\bar{\mathbf{s}}_1 = \left[\mathbf{s}_1^T\ \mathbf{0}_{1\times(L-1)}\right]^T \tag{10}$$

$$\bar{\mathbf{s}}_2 = \left[\mathbf{s}_2^T\ \mathbf{0}_{1\times(L-1)}\right]^T \tag{11}$$

such that the $(2L-1)\times 1$ discretized frequency response is

$$\bar{\mathbf{s}}_{1,\mathrm{f}} = \mathbf{A}^H \bar{\mathbf{s}}_1 \tag{12}$$

$$\bar{\mathbf{s}}_{2,\mathrm{f}} = \mathbf{A}^H \bar{\mathbf{s}}_2, \tag{13}$$

for $\mathbf{A}^H$ the $(2L-1)\times(2L-1)$ discrete Fourier transform (DFT) matrix, $\mathbf{A}$ the inverse DFT, and $(\bullet)^H$ the Hermitian. The corresponding nonlinear waveforms can thus also be written as

$$\bar{\mathbf{s}}_{12} = \bar{\mathbf{s}}_1 \odot \bar{\mathbf{s}}_2 \tag{14}$$

$$\bar{\mathbf{s}}_{11} = \bar{\mathbf{s}}_1 \odot \bar{\mathbf{s}}_1 \tag{15}$$

$$\bar{\mathbf{s}}_{22} = \bar{\mathbf{s}}_2 \odot \bar{\mathbf{s}}_2 \tag{16}$$

$$\bar{\mathbf{s}}_{12,\mathrm{f}} = \mathbf{A}^H \bar{\mathbf{s}}_{12} \tag{17}$$

$$\bar{\mathbf{s}}_{11,\mathrm{f}} = \mathbf{A}^H \bar{\mathbf{s}}_{11} \tag{18}$$

$$\bar{\mathbf{s}}_{22,\mathrm{f}} = \mathbf{A}^H \bar{\mathbf{s}}_{22}\,. \tag{19}$$

The $(2L-1)\times 1$ discretized autocorrelation of $\bar{\mathbf{s}}_{12}$ can therefore be written as

$$\begin{aligned}\mathbf{r} &= \mathbf{A}\left|\bar{\mathbf{s}}_{1,\mathrm{f}} \odot \bar{\mathbf{s}}_{2,\mathrm{f}}\right|^2 \\ &= \mathbf{A}\{\,[\mathbf{A}^H(\bar{\mathbf{s}}_1 \odot \bar{\mathbf{s}}_2)] \odot [\mathbf{A}^H(\bar{\mathbf{s}}_1 \odot \bar{\mathbf{s}}_2)]^*\},\end{aligned} \tag{20}$$

for $(\bullet)^*$ complex conjugation, and the $(2L-1)\times 1$ discretized cross-correlations between $\bar{\mathbf{s}}_{12}$ and $\bar{\mathbf{s}}_{11}$, $\bar{\mathbf{s}}_{22}$ can be written as

$$\mathbf{c}_1 = \mathbf{A}\{\,[\mathbf{A}^H(\bar{\mathbf{s}}_1 \odot \bar{\mathbf{s}}_2)] \odot [\mathbf{A}^H(\bar{\mathbf{s}}_1 \odot \bar{\mathbf{s}}_1)]^*\} \tag{21}$$

$$\mathbf{c}_2 = \mathbf{A}\{\,[\mathbf{A}^H(\bar{\mathbf{s}}_1 \odot \bar{\mathbf{s}}_2)] \odot [\mathbf{A}^H(\bar{\mathbf{s}}_2 \odot \bar{\mathbf{s}}_2)]^*\}. \tag{22}$$

To minimize the sidelobes of (20) while also minimizing the cross-correlations of (21) and (22), we modify the generalized integrated sidelobe level (GISL) metric from [23] that operates on the p-norm ratio of the sidelobes to the mainlobe and subsumes both ISL ($p = 2$) and PSL ($p = \infty$) as special cases. This new cost function is defined as

$$J = \left[\frac{\|\mathbf{w}_{\mathrm{SL}} \odot \mathbf{r}\|_p^p + \|\mathbf{c}_1\|_p^p + \|\mathbf{c}_2\|_p^p}{\|\mathbf{w}_{\mathrm{ML}} \odot \mathbf{r}\|_p^p}\right]^{1/p} \tag{23}$$

where $\|\bullet\|_p$ is the p-norm and the $(2L-1)\times 1$ vectors $\mathbf{w}_{\mathrm{SL}}$ and $\mathbf{w}_{\mathrm{ML}}$ extract the sidelobes and mainlobe of the autocorrelation $\mathbf{r}$, respectively. For an "over-sampling" factor of K, the null-to-null width of the mainlobe comprises the $2K-1$ samples in the center of $\mathbf{r}$, with $\mathbf{w}_{\mathrm{SL}}$ and $\mathbf{w}_{\mathrm{ML}}$ constructed accordingly. It was shown in [24] that setting the mainlobe width in this manner likewise effectively establishes the 3-dB bandwidth of the intermodulation. For convenience, we define the components

$$\begin{aligned} J_1 &= \|\mathbf{w}_{\mathrm{SL}} \odot \mathbf{r}\|_p^p \\ J_2 &= \|\mathbf{c}_1\|_p^p \\ J_3 &= \|\mathbf{c}_2\|_p^p \\ J_4 &= \left(\|\mathbf{w}_{\mathrm{SL}} \odot \mathbf{r}\|_p^p + \|\mathbf{c}_1\|_p^p + \|\mathbf{c}_2\|_p^p\right)^{1/p} \\ J_5 &= \left(\|\mathbf{w}_{\mathrm{ML}} \odot \mathbf{r}\|_p^p\right)^{1/p}. \end{aligned} \tag{24}$$

The $N\times 1$ gradient with respect to each code $\mathbf{x}_1$ and $\mathbf{x}_2$ is

$$\nabla_{\mathbf{x}_1} = \left[\frac{\partial}{\partial\alpha_{1,1}}\ \frac{\partial}{\partial\alpha_{1,2}}\ \cdots\ \frac{\partial}{\partial\alpha_{1,N}}\right]^T \tag{25}$$

$$\nabla_{\mathbf{x}_2} = \left[\frac{\partial}{\partial\alpha_{2,1}}\ \frac{\partial}{\partial\alpha_{2,2}}\ \cdots\ \frac{\partial}{\partial\alpha_{2,N}}\right]^T. \tag{26}$$

If (25) is applied to (23), using (24), then we obtain

$$\begin{aligned}\nabla J_{1_{\mathbf{x}_1}} = 2\mathrm{p}\bar{\mathbf{B}}^T\, \Im\Big\{&(\bar{\mathbf{s}}_1^* \odot \bar{\mathbf{s}}_2^*) \\ &\odot \Big[\mathbf{A}\,[\mathbf{A}^H(\bar{\mathbf{s}}_1 \odot \bar{\mathbf{s}}_2) \\ &\odot \mathbf{A}^H(\mathbf{w}_{\mathrm{SL}} \odot |\mathbf{r}|^{p-2} \odot \mathbf{r})]\Big]\Big\}\end{aligned}$$

$$\begin{aligned}\nabla J_{2_{\mathbf{x}_1}} = 2\mathrm{p}\bar{\mathbf{B}}^T \times \\ \Im\left\{\left[\begin{array}{l}(\bar{\mathbf{s}}_1^* \odot \bar{\mathbf{s}}_1^*) \odot \left(\mathbf{A}\,[\mathbf{A}^H(\bar{\mathbf{s}}_1 \odot \bar{\mathbf{s}}_2) \odot \mathbf{A}^{\mathrm{H}}(|\mathbf{c}_1|^{p-2} \odot \mathbf{c}_1^*)]\right) \\ +\frac{1}{2}(\bar{\mathbf{s}}_1^* \odot \bar{\mathbf{s}}_2^*) \odot \left(\mathbf{A}\,[\mathbf{A}^H(\bar{\mathbf{s}}_1 \odot \bar{\mathbf{s}}_1) \odot \mathbf{A}^{\mathrm{H}}(|\mathbf{c}_1|^{p-2} \odot \mathbf{c}_1)]\right)\end{array}\right]\right\}\end{aligned}$$

$$\begin{aligned}\nabla J_{3_{\mathbf{x}_1}} = \mathrm{p}\bar{\mathbf{B}}^T\, \Im\Big\{&(\bar{\mathbf{s}}_1^* \odot \bar{\mathbf{s}}_2^*) \\ &\odot \left(\mathbf{A}\,[\mathbf{A}^H(\bar{\mathbf{s}}_2 \odot \bar{\mathbf{s}}_2) \right. \\ &\left. \odot \mathbf{A}^H(|\mathbf{c}_2|^{p-2} \odot \mathbf{c}_2)]\right)\Big\}\end{aligned}$$

$$\nabla J_{4_{\mathbf{x}_1}} = \left(\frac{1}{p}\right)[J_1 + J_2 + J_3]^{1/p-1}\left[\nabla J_{1_{\mathbf{x}_1}} + \nabla J_{2_{\mathbf{x}_1}} + \nabla J_{3_{\mathbf{x}_1}}\right]$$

$$\nabla J_{5_{\mathbf{x}_1}} = 2\left(\frac{J_5}{J_5^p}\right)\bar{\mathbf{B}}^T \Im\{(\bar{\mathbf{s}}_1^* \odot \bar{\mathbf{s}}_2^*) \odot (\mathbf{A}\,[\mathbf{A}^H(\bar{\mathbf{s}}_1 \odot \bar{\mathbf{s}}_2) \odot \mathbf{A}^H(\mathbf{w}_{\mathrm{ML}} \odot |\mathbf{r}|^{p-2} \odot \mathbf{r})])\}$$

$$\nabla J_{\mathbf{x}_1} = \frac{(J_5)\left(\nabla J_{4_{\mathbf{x}_1}}\right) - (J_4)\left(\nabla J_{5_{\mathbf{x}_1}}\right)}{J_5^2}. \quad (27)$$

Here the matrix $\mathbf{B}$ has likewise been appended with $L-1$ rows of zeros as

$$\bar{\mathbf{B}} = \left[\mathbf{B}^T\ \mathbf{0}_{N\times(L-1)}\right]^T, \quad (28)$$

$\Im\{\bullet\}$ is the imaginary part of the argument, and $|\bullet|^{p-2}$ applies an element-wise absolute value and element-wise exponent. A similar result, albeit in terms of $\mathbf{x}_2$, is obtained when (26) is applied to (23). The final overall gradient is therefore the concatenation $\nabla J_{\mathbf{x}} = \left[\nabla J_{\mathbf{x}_1}^T\ \nabla J_{\mathbf{x}_2}^T\right]^T$. With the gradients expressed in this manner they can be efficiently computed using fast Fourier transforms (FFTs) and vector/matrix multiplies [25, 26].

The generic descent optimization update for $\tilde{\mathbf{x}} = [\mathbf{x}_1^T\ \mathbf{x}_2^T]^T$ at the i^{th} iteration is

$$\tilde{\mathbf{x}}_{i+1} = \tilde{\mathbf{x}}_i + \mu_i\,\mathbf{p}_i \quad (29)$$

for $\mathbf{p}_i$ the current descent direction and μ_i the associated step size. Here, the descent direction is updated using the heavy-ball gradient descent method [27] that uses a combination of the current and past gradients and is known to converge faster than standard gradient descent.

III. Simulated and Experimental Results

The properties of an intermodulation waveform $\mathbf{s}_{12}$ produced from a pair of PRO-FM waveforms (the approach from [7]) is compared to that produced by a pair of waveforms realized by the joint SSPRInt (J-SSPRInt) formulation above. The relationship that $\mathbf{s}_{12}$ has with the two harmonic waveforms $\mathbf{s}_{11}$ and $\mathbf{s}_{22}$ is considered in each case.

Each PRO-FM waveform is optimized to have a fundamental time-bandwidth product of $BT = 50$, resulting in an associated intermodulation waveform with $BT \cong 72$ and harmonics with $BT \cong 124$. The J-SSPRInt waveform pair is optimized according to the 2nd order nonlinear characteristics and thus the associated intermodulation response is designed to have $BT = 50$ while the harmonics have $BT \cong 100$.

A. Simulation Results

Figures 1 and 2 illustrate the autocorrelation $\mathbf{r}$ of a single $\mathbf{s}_{12}$ intermodulation pair as well as the corresponding cross-correlations $\mathbf{c}_1$ and $\mathbf{c}_2$ for PRO-FM and J-SSPRInt waveforms, respectively. Note that this result does not account for the phenomenological scaling of the harmonic and intermodulation responses, where the former would otherwise tend to mask the latter due to the transmitter(s) generating harmonics as well.

However, when 100,000 unique PRO-FM or J-SSPRInt waveform pairs are produced, the coherently integrated correlations shown in Figs. 3 and 4 are realized. Specifically, it is observed that the cross-correlation responses have been reduced by around 50 dB in both cases, which is in line with the incoherent sidelobe suppression of 10 $\log_{10}(100{,}000)$.

The mean power spectrum of $\mathbf{s}_{12}$, $\mathbf{s}_{11}$, and $\mathbf{s}_{22}$ over each set of 100,000 waveform pairs is shown in Figs. 5 and 6. In the latter it is interesting to note that, in agreement with the cross-spectrum form of the Wiener-Khintchine theorem, the waveform pairs obtained by J-SSPRInt realize a 3.5 dB notch (relative to the harmonic peak power) that coincides with the peak of the intermodulation spectrum. Thus, an improved separation between the harmonic and intermodulation responses are observed relative to the PRO-FM case of Fig. 5.

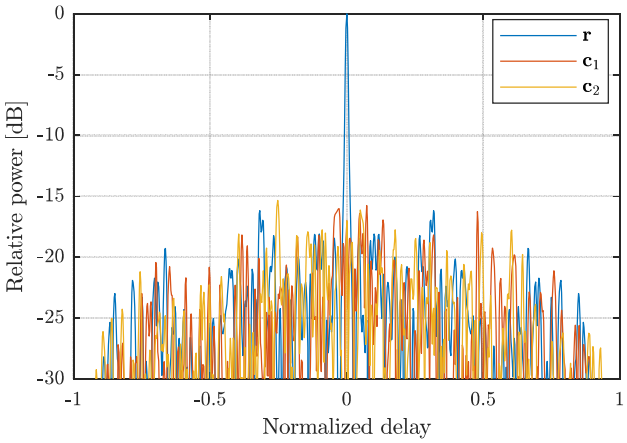

Fig. 1: Simulated correlations between the modeled intermodulation $\mathbf{s}_{12}$ and harmonics $\mathbf{s}_{11}$ and $\mathbf{s}_{22}$ for a single pair of PRO-FM waveforms

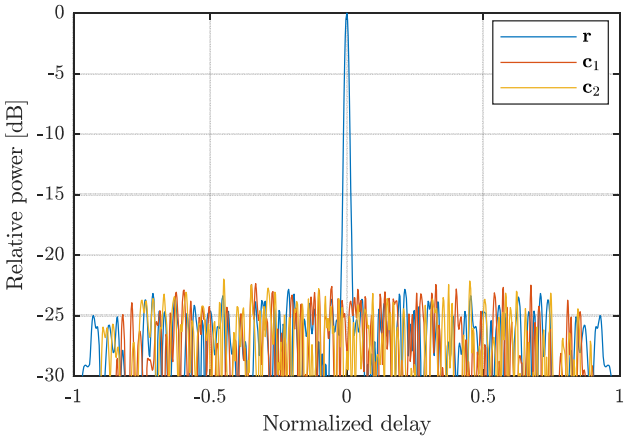

Fig. 2: Simulated correlations between the modeled intermodulation $\mathbf{s}_{12}$ and harmonics $\mathbf{s}_{11}$ and $\mathbf{s}_{22}$ for a single pair of J-SSPRInt waveforms

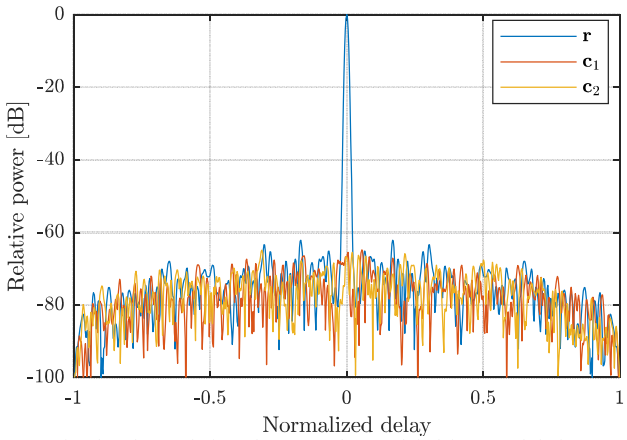

Fig. 3: Simulated correlations between the modeled intermodulation $\mathbf{s}_{12}$ and harmonics $\mathbf{s}_{11}$ and $\mathbf{s}_{22}$ integrated over 100,000 pairs of PRO-FM waveforms

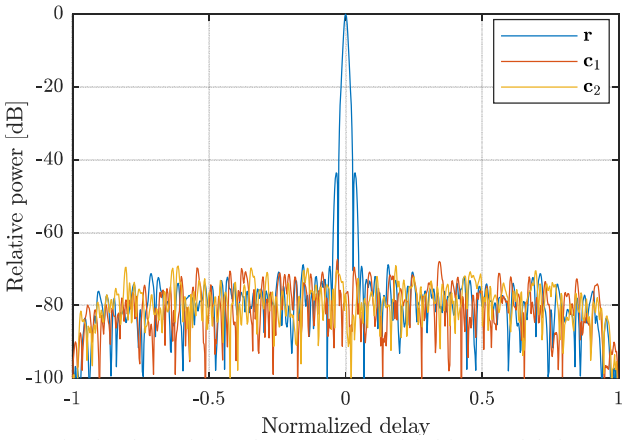

Fig. 4: Simulated correlations between the modeled intermodulation $\mathbf{s}_{12}$ and harmonics $\mathbf{s}_{11}$ and $\mathbf{s}_{22}$ integrated over 100,000 pairs of J-SSPRInt waveforms

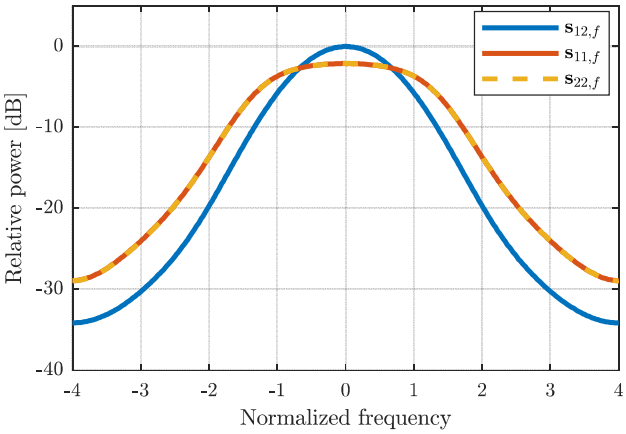

Fig. 5: Mean power spectrum of $\mathbf{s}_{12}$, $\mathbf{s}_{11}$, and $\mathbf{s}_{22}$ for a set of 100,000 PRO-FM waveform pairs

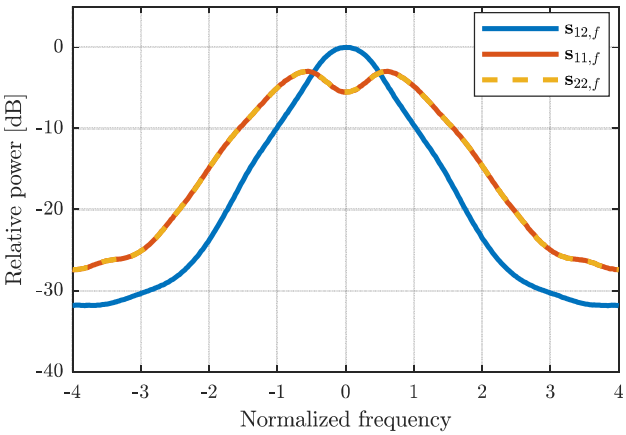

Fig. 6: Mean power spectrum of $\mathbf{s}_{12}$, $\mathbf{s}_{11}$, and $\mathbf{s}_{22}$ for a set of 100,000 J-SSPRInt waveform pairs

To better visualize the difference in performance between these two waveform sets, Fig. 7 shows the root mean squared (RMS) correlations of $\mathbf{s}_{12}$, $\mathbf{s}_{11}$, and $\mathbf{s}_{22}$ for 100 unique sets of the mean response from 1000 waveform pairs. It is observed that, disregarding the close-in shoulder lobes, the J-SSPRInt waveform pairs provide about 5 dB improvement over the separately designed PRO-FM waveform pairs. A small cross-correlation peak occurs for the PRO-FM pairs, though it does de-cohere when integrating over all 100,000 pairs coherently.

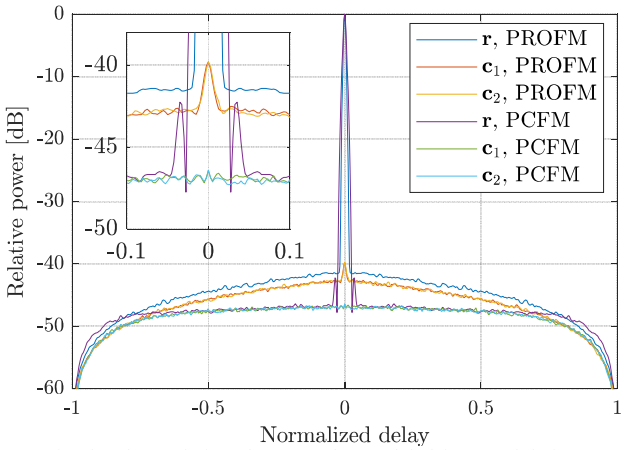

Fig. 7: Simulated correlations between the modeled intermodulation $\mathbf{s}_{12}$ and harmonics $\mathbf{s}_{11}$ and $\mathbf{s}_{22}$ when integrating the magnitude over 100 unique sets of coherent combinations of 1000 PRO-FM and J-SSPRInt waveform pairs.

B. Experimental Results

We now evaluate J-SSPRInt experimentally in a loopback configuration. The same 100,000 pairs of J-SSPRInt and PRO-FM waveforms are individually tested. Each waveform pair is implemented using separate channels of a Tektronix AWG70002A arbitrary waveform generator (AWG) at a center frequency of 900 MHz and a pulse repetition interval (PRI) of 4 μs, such that the total coherent processing interval (CPI) is 0.4 s. All fundamental waveforms have 3-dB bandwidths of 25 MHz and 2 μs pulsewidths. The image signals produced by the AWG are suppressed with MiniCircuits SLP-1000+ lowpass filters. Each waveform pair is then amplified by a separate MiniCircuits TVA-82-213 amplifier that produces the harmonic waveforms $s_{11}(t)$ and $s_{22}(t)$.

Each amplifier output is separated into a low frequency (850-950 MHz) and high frequency (1700-1900 MHz) band, corresponding respectively to each fundamental and second order harmonic, using two Mini-Circuits RDP-272+ diplexers. The RF chain is then split into the following three paths: 1) the high frequency band of the first amplifier $s_{11}(t)$ is attenuated, 2) the high frequency band of the second amplifier $s_{22}(t)$ is attenuated, 3) the low frequency bands of each amplifier are attenuated, combined using a MiniCircuits ZAPD-2-21-3W power combiner, and injected into the nonlinear device under test (DUT), which in this context is a powered MiniCircuits ZFL-2000G+ wideband amplifier. The resulting intermodulation signal $s_{12}(t)$ is then variably attenuated and recombined with both harmonics $s_{11}(t)$ and $s_{22}(t)$ using a Broadway Technologies 151-040-008 power combiner. Unused inputs are terminated with loads. The RF chain is arranged in this way to improve isolation and control of the signal-to-interference ratio between the intermodulation and the harmonic components for analysis purposes.

At the receiver, the linear responses are highpass filtered using two MiniCircuits RDP-272+ diplexers in series, with the low frequency ports terminated, such that nonlinearities generated within the receiver are mitigated. Without these filters, detection of the DUT nonlinear scattering would be

limited by the second-order intermodulation and filter rejection of the receiver at the fundamental frequency. Following the two diplexers in the "receive" chain, the harmonic and intermodulation components are amplified with a MiniCircuits ZX60-33LN-S+. The resulting I/Q data is captured at a center frequency of 1800 MHz and sample rate of 200 MHz using a Rohde & Schwarz spectrum analyzer. This test setup is depicted in Figs. 8 and 9.

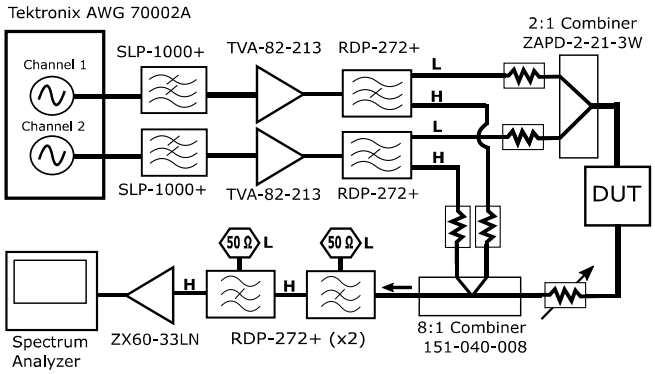

Fig. 8: Hardware setup for the J-SSPRInt loopback experiment

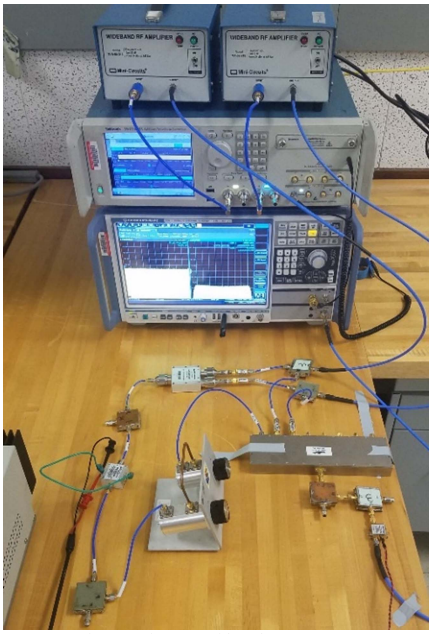

Fig. 9: Picture of hardware setup

To determine the accuracy of the nonlinear power series approximation used to model the intermodulation waveform for matched filtering, as well as the ability to coherently integrate the autocorrelations resulting from both waveform sets, paths 1 and 2 are disconnected from the combiner and terminated with a matched load so that only the intermodulation on path 3 is received. Figure 10 shows the normalized correlation between the power series approximation of $s_{12}(t)$ and the measured intermodulation data for 100,000 coherently averaged pulse pairs. Mismatch losses of −2.3 dB and −2.6 dB are observed between the measured DUT response and the modeled power series approximation for the PRO-FM and J-SSPRInt waveform pairs, respectively. As expected, the intermodulation autocorrelation mainlobe experiences a substantial coherent gain and sidelobes are incoherently suppressed in both cases.

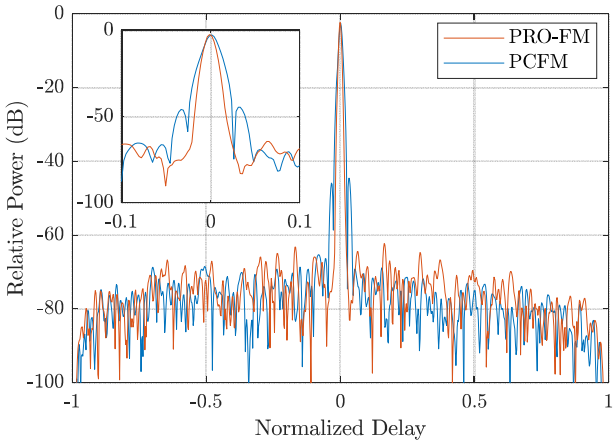

Fig. 10: Experimentally measured nonlinear response using the power series approximation of $s_{12}(t)$ as matched filter when only the intermodulation signal is present for 100,000 PRO-FM and J-SSPRInt waveform pairs

To verify that the power series approximation for $s_{12}(t)$ is uncorrelated with the unintentional "transmitter" harmonics generated by the TVA amplifier for the J-SSPRInt waveforms, paths 1 and 2 are connected to the combiner while path 3 is disconnected and terminated such that no intermodulation is present. Figure 11 shows the correlation response between the harmonic measurements with the corresponding modeled matched filter for $s_{12}(t)$ overlaid with the corresponding results of Figure 10 for 100,000 responses coherently averaged. This result clearly shows that, with sufficiently unique waveforms, the harmonic responses can be made highly uncorrelated with the desired intermodulation response.

Finally, all three paths are connected and the variable attenuator of path 3 used to control the SIR between the intermodulation signal and the total harmonic power. Figure 12 shows the result when the combined intermodulation/harmonic measurement is matched filtered with the power series approximation and then coherently averaged for 100,000 waveform pairs. For an SIR of −60 dB the intermodulation response can still be recovered despite being masked by significant harmonic interference power.

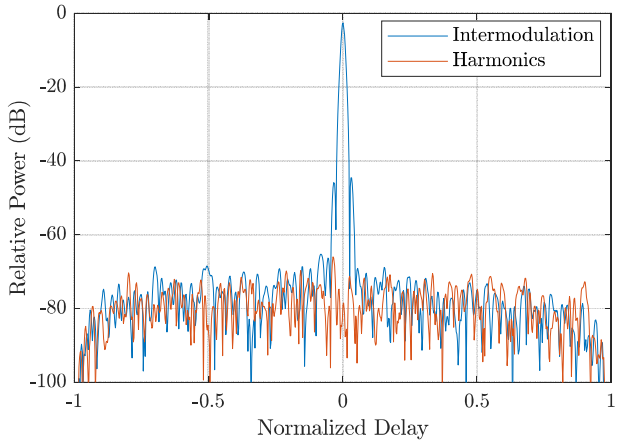

Fig. 11: Response of the experimental harmonic measurement to the matched filtered from the power series approximation for 100,000 J-SSPRInt waveform pairs. Compared with matched filtered intermodulation response from Fig. 10.

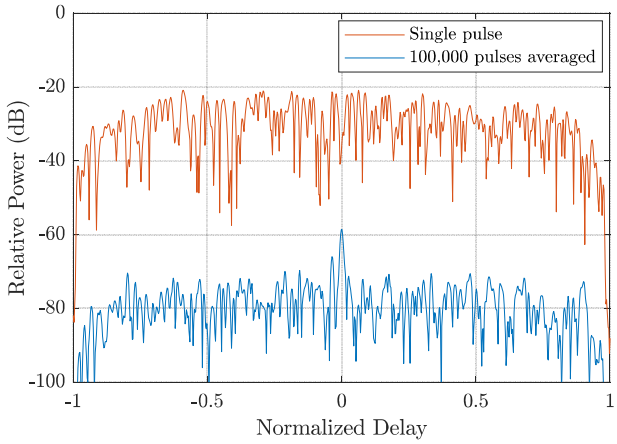

Fig. 12: Measurement containing both intermodulation and harmonic responses matched filtered with the power series approximation and coherent averaged for 100,000 J-SSPRInt waveform pairs

IV. Conclusions

Leveraging recent work on the intermodulation of FM noise waveform pairs, it was shown here that joint optimization of the waveform pairs for the purpose of minimizing the correlation between the intermodulation and waveform harmonics can provide a few dB additional receive separation. It remains to be seen just how much additional benefit joint optimization can realize for free-space operation, though the tremendous gains that these random waveforms facilitate in general does underscore the potential for this form of nonlinear radar.

References

[1] R.O. Harger, "Harmonic radar systems for near-ground in-foliage nonlinear scatterers," *IEEE Trans. Aerospace & Electronic Systems*, vol. AES-12, no. 2, pp. 230-245, Mar. 1976.

[2] G.J. Mazzaro, A.F. Martone, K.I. Ranney, R.M. Narayanan, "Nonlinear radar for finding RF electronics: system design and recent advancements," *IEEE Trans. Microwave Theory & Techniques*, vol. 65, no. 5, pp. 1716-1726, May 2017.

[3] K.A. Gallagher, G.J. Mazzaro, R.M. Narayanan, K.D. Sherbondy, A.F. Martone, "Automated cancellation of harmonics using feed-forward filter reflection for radar transmitter linearization," *Proc. SPIE 9077, Radar Sensor Technology XVIII*, May 2014.

[4] A.F. Martone, E.J. Delp, "Characterization of RF devices using two-tone probe signals," *IEEE Workshop on Statistical Signal Processing*, Madison, WI, Sept. 2007.

[5] G.J. Mazzaro, A.F. Martone, D.M. McNamara, "Detection of RF electronics by multitone harmonic radar," *IEEE Trans. Aerospace & Electronic Systems*, vol. 50, no. 1, pp. 477-490, Jan. 2014.

[6] G.J. Mazzaro, K.A. Gallagher, A.F. Martone, K.D. Sherbondy, R.M. Narayanan, "Short-range harmonic radar: chirp waveform, electronic targets," *Proc. SPIE 9461, Radar Sensor Technology XIX and Active and Passive Signatures VI*, May 2015.

[7] J. Owen, S. D. Blunt, K. Gallagher, P. McCormick, C. Allen, K. Sherbondy, "Nonlinear radar via intermodulation of FM noise waveform pairs," *IEEE Radar Conf.*, Oklahoma City, OK, Apr. 2018.

[8] J. Jakabosky, S.D. Blunt, B. Himed, "Waveform design and receive processing for nonrecurrent nonlinear FMCW radar," *IEEE Intl. Radar Conf.*, Arlington, VA, May 2015.

[9] J. Jakabosky, S.D. Blunt, B. Himed, "Spectral-shape optimized FM noise radar for pulse agility," *IEEE Radar Conf.*, Philadelphia, PA, May 2016.

[10] S.D. Blunt, E.L. Mokole, "An overview of radar waveform diversity," *IEEE Aerospace & Electronic Systems Mag.*, vol. 31, no. 11, pp. 2-42, Nov. 2016.

[11] S.R.J. Axelsson, "Noise radar using random phase and frequency modulation," *IEEE Trans. Geoscience & Electronic Systems*, vol. 42, no. 11, pp. 2370-2384, Nov. 2004.

[12] L. Pralon, B. Pompeo, J.M. Fortes, "Stochastic analysis of random frequency modulated waveforms for noise radar systems," *IEEE Trans. Aerospace & Electronic Systems*, vol. 51, no. 2, pp. 1447-1461, Apr. 2015.

[13] L. Pralon, G. Beltrao, B. Pompeo, M. Pralon, J.M. Fortes, "Near-thumbtack ambiguity function of random frequency modulated signals," *IEEE Radar Conf.*, Seattle, WA, May 2017.

[14] B. Ravenscroft, J.W. Owen, J. Jakabosky, S.D. Blunt, A.F. Martone, K.D. Sherbondy, "Experimental demonstration and analysis of cognitive spectrum sensing & notching," *IET Radar, Sonar & Navigation*, vol. 12, no. 12, pp. 1466-1475, Dec. 2018.

[15] G. Zook, P.M. McCormick, S.D. Blunt, C. Allen, J. Jakabosky, "Dual-polarized FM noise radar," *IET Intl. Conf. Radar Systems*, Belfast, UK, Oct. 2017.

[16] G. Zook, P. McCormick, S.D. Blunt, "Fixational eye movement radar: random spatial modulation," *IEEE Radar Conf.*, Oklahoma City, OK, Apr. 2018.

[17] C.A. Mohr, P.M. McCormick, S.D. Blunt, "Optimized complementary waveform subsets within an FM noise radar CPI," *IEEE Radar Conf.*, Oklahoma City, OK, Apr. 2018.

[18] B. Ravenscroft, P.M. McCormick, S.D. Blunt, E. Perrins, J.G. Metcalf, "A power-efficient formulation of tandem-hopped radar & communications," *IEEE Radar Conf.*, Oklahoma City, OK, Apr. 2018

[19] S.A. Maas, *Nonlinear Microwave Circuits*, Artech House, 1988.

[20] F. Giannini, *Nonlinear Microwave Circuit Design*, John Wiley & Sons, 2004.

[21] J.C. Pedro, N.B. Carvolho, *Intermodulation Distortion in Microwave and Wireless Circuits*, Artech House, 2003.

[22] S.D. Blunt, M. Cook, J. Jakabosky, J. de Graaf, E. Perrins, "Polyphase-coded FM (PCFM) radar waveforms, part I: implementation," *IEEE Trans. Aerospace & Electronic Systems*, vol. 50, no. 3, pp. 2218-2229, July 2014.

[23] P.M. McCormick, S.D. Blunt, "Nonlinear conjugate gradient optimization of polyphase-coded FM radar waveforms," *IEEE Radar Conf.*, Seattle, WA, May 2017.

[24] P.M. McCormick, S.D. Blunt, "Gradient-based coded-FM waveform design using Legendre polynomials," *IET Intl. Radar Conf.*, Belfast, UK, Oct. 2017.

[25] B. O'Donnell, J.M. Baden, "Fast gradient descent for multi-objective waveform design," *IEEE Radar Conf.*, Philadelphia, PA, May 2016.

[26] D. Zhao, Y. Wei, Y. Liu, "Spectrum optimization via FFT-based conjugate gradient method for unimodular sequence design," *Signal Processing*, vol. 142, pp. 354-365, Jan. 2018.

[27] J. Nocedal, S. Wright, *Numerical optimization*, Springer Science & Business Media, 2006.